Research Article

Fracture toughness of a rejuvenated β-Ti reinforced bulk metallic glass matrix composite

Devashish Rajpoot [1,2], R. Lakshmi Narayan [3,*], Long Zhang [4,*], Punit Kumar [2], Haifeng Zhang [4], Parag Tandaiya [1], Upadrasta Ramamurty [2,5]

[1] Department of Mechanical Engineering, Indian Institute of Technology Bombay, Powai, Mumbai 400076, India
[2] Department of Mechanical and Aerospace Engineering in Nanyang Technological University, Singapore 637331, Republic of Singapore
[3] Department of Materials Science and Engineering, Indian Institute of Technology Delhi, Hauz Khas, New Delhi 110016, India
[4] Shi-changxu Innovation Center for Advanced Materials, Institute of Metal Research, Chinese Academy of Sciences, Shenyang 110016, China
[5] Institute of Materials Research and Engineering, Agency for Science, Technology and Research (A ∗STAR), Singapore 138634

*Corresponding authors: Prof., R. Lakshmi Narayan; Tel.: +91 11 26591494; Dr. Long Zhang; Tel.: +86-24-83970248

Email address: rlnarayan@mse.iitd.ac.in (R. Lakshmi Narayan); zhanglong@imr.ac.cn (Long Zhang)

Abstract: A β-Ti dendrite reinforced Zr-based bulk metallic glass composite (BMGC) was found to be brittle when cast in a large size. The reasons for the embrittlement and the effectiveness of the cryothermal cycling (CTC) treatment in restoring the mode I fracture toughness are examined. Plasticity in all the CTC treated BMGC is estimated from the distribution and occurrence of pop-ins in nanoindentation tests and by measuring the magnitude of enthalpy of relaxation (ΔH_{rel}) via differential scanning calorimetry (DSC). This is further validated by examining the strain-to-failure (ε_f) in compression tests. Mode I fracture behaviour of the as-cast embrittled BMGC and the CTC treated BMGC, which exhibits maximum plasticity, is examined. Results show that both BMGCs are equally brittle and exhibit 5 times lower notch toughness (K_{QJ}) than their tougher counterpart. Post-facto imaging of the side surfaces reveals the absence of notch-tip plasticity in both BMGCs. The lack of notch tip plasticity of CTC treated BMGC, despite exhibiting signatures of plasticity in nanoindentation

and higher ΔH_{rel} is rationalized by reassessing the origin of pop-ins in nanoindentation tests and describing the variations in chemical and topological short range ordering during CTC, respectively. Implications of these results in terms of improving the fracture toughness of structurally relaxed BMGCs via CTC are discussed.

Keywords: Bulk metallic glass composites; Fracture; Rejuvenation; Shear bands; Microsegragation.

1. Introduction

Bulk metallic glasses (BMGs) exhibit negligible ductility, in uniaxial tension and at temperatures well below their glass transition temperature, T_g, as they undergo plastic deformation mediated by shear bands, which in the absence of an interacting microstructure propagate unhindered and cause failure [1–9] . To enhance ductility, a composite approach is adopted, wherein a ductile crystalline phase is introduced in the BMG matrix [1,10–23]. One of the popular means of fabricating such BMG matrix composites (BMGCs) is to choose a composition that undergoes phase separation into amorphous and crystalline phases during solidification from the melt [12–14,16–22,24–26]. Of the several such BMGCs, the ones with β-Ti dendrites in a Zr/Ti-based metallic glass matrix are promising as they exhibit excellent ductility, without a significant trade-off in strength [13,19–21,25,27,28]. Moreover, the size, volume fraction, and metastability of the dendrites can be tailored to achieve the desired combination of strength and ductility [19]. Recognizing that the fracture toughness, K_{IC}, rather than ductility, is the key engineering parameter gauging the structural integrity of glasses, the fracture behaviour of these BMGCs were recently examined [29]. It was reported that K_{IC} of the BMGC referred to as DH3 is ~157 MPa. $m^{0.5}$, which is 3-5 times higher than that of most Zr-based BMGs [29–31].

In a recent study, we observed that the structural state of the amorphous matrix also affects the fracture behavior of of β-Ti reinforced BMGCs [32]. If the amorphous matrix is structurally relaxed, its ability to undergo plastic deformation diminishes markedly, leading to a precipitous drop in K_{IC}. Structural relaxation occurs when the amorphous matrix in BMGCs is

exposed to elevated temperatures, close to T_g, for extended periods of time or when the BMGC melt solidifies at lower cooling rates. Such a situation is encountered in large castings, where the cooling rate at the centre of the casting is likely to be significantly lower than that at the surface. This imposes a restriction on the size to which a BMGC can be cast, which in turn, limits its use in large scale structural applications.

In view of this, there is a need to explore strategies that can re-toughen a BMGC that has undergone structural relaxation-induced embrittlement. Recent studies indicate that the plasticity of BMGs can be enhanced by different types of rejuvenation processes, such as elasto-static loading, ion irradiation, plastic deformation, and cryothermal cycling (CTC) [4,33–39]. Of these, CTC is most preferred as it is simple, requires a low-cost setup and can be adapted to large scale processing [40]. A significant enhancement in plasticity is observed only when the BMG is subjected to a specific number of CTC cycles, which in turn depends on its composition. Ketkaew et al. [41] and Li et al. [42] performed CTC on different BMGs and reported that even K_{IC} of some Zr-based BMGs increase by 50% after 200 and 70 cycles, respectively. However, it is noted that CTC treatments in these studies were performed on BMGs that were reasonably tough to begin with, i.e. they had not undergone structural relaxation-induced embrittlement. Therefore, it is not clear if the CTC treatment can rejuvenate the BMG matrix of a structurally relaxed BMGC and enhance its K_{IC}.

Keeping this in view, we fabricated a β-Ti reinforced BMGC in bar and ingot forms. Uniaxial tensile tests indicate that the former exhibits significant ductility whereas the latter is brittle. The ingot specimens were subjected to CTC to determine the appropriate number of CTC cycles required for maximizing its plasticity. Mode I fracture experiments are conducted to assess if the toughness can be enhanced by recourse to rejuvenation. Results of these tests are compared with those of the as-cast bar specimen, which are reported in our previous study [32]. It is observed that both BMGCs are considerably brittle and exhibit negligible crack tip plasticity. To rationalize these results, the structural evolution of the BMG matrix, in terms of chemical and topological short-range ordering is analyzed, and its influence on enhancing plasticity is discussed. Finally, the implications of employing CTC as a potential rejuvenation treatment to enhance K_{IC} of BMGs and BMGCs are critically assessed.

2. Materials and experiments

2.1. Materials

A Zr-based BMGC, with the composition $Zr_{39.6}Ti_{33.9}Cu_{6.4}Nb_{7.6}Be_{12.5}$ (at.%) is examined in this study. This composition corresponds to that of DH3, which is widely studied in the literature and reported to be one of the toughest BMGC [13,22,29,32]. Two different types of it were examined: bar and ingot forms, both of which were arc melted. While the 'bar' specimens are cast into 45 mm × 12 mm × 5 mm (length × breadth × thickness) molds, the 'ingot' specimens into molds that are 15 mm in thickness and 45 mm in diameter. For microstructural investigations, smaller cuboid specimens (edge length: 4 mm) are sectioned from each stock using wire-cut electrical discharge machining (EDM). These specimens are ground and mechanically polished to a mirror-like surface finish. Microstructure analysis is performed with a field emission scanning electron microscope (FESEM) JEOL 7600 and the chemical compositions are measured using the energy dispersive X-ray spectroscopy (EDS) feature attached with it. Malvern Panalytical X-ray diffractometer is used for performing X-ray diffraction (XRD) on the specimens. Small pieces are sectioned from the ingot to perform differential scanning calorimetry (TA Q100 DSC). The heating and cooling rates employed for DSC measurements are both 20 K/min. A minimum of 3 tests are performed on each condition. Specimens extracted from the ingot were subjected to predetermined number of thermal cycles (5, 10, 20, 30, and 60) by alternatingly immersing them in liquid nitrogen (77 K), and ethanol (held at 300 K), for 1 min each. The temperatures of liquid nitrogen and ethanol were monitored via thermocouples. Since the thermal conductivity of the BMGC is reasonably high, the soaking time of 1 min is sufficient for equilibrating the specimen at the chosen temperatures. Note that CTC is not performed on specimens extracted from the bar stock. DSC measurements are also performed on all ingot specimens subjected to CTC.

2.2. Mechanical characterization

Nanoindentation experiments are performed on specimens extracted from the as-cast bar and ingot specimens, as well as those subjected to CTC. The Nanoindenter XP instrument (Keysight

Technologies, Oak Ridge, TN, USA), which is equipped with a spherical diamond indenter tip that has a radius, R_i = 5 μm, was used for this purpose. A maximum load, P_{max}, of ~30 mN is applied, and both the loading and unloading rates are maintained at 0.5 mN/s. 20 nanoindentations are performed at different locations in each specimen. Additionally, Vickers microindentations on the same specimens are performed using a maximum load of 10 N.

Uniaxial tensile specimens with dimensions 6 mm × 2 mm × 0.6 mm (gauge length × width × thickness) and compression specimens with a diameter ~2.2 mm and aspect ratio of 2 are extracted from the ingots, in as-cast and CTC condition. For the as-cast bars, only compression specimens are extracted as their uniaxial tensile test data is already reported by us [32]. Three specimens for each condition are tested to ensure repeatability. Tensile tests are conducted at a quasistatic strain rate of 0.001 s^{-1} in a ZwickRoell micro-tensile testing machine attached with a 120 pixel/mm resolution laser extensometer. The compression tests are conducted using a Shimadzu universal testing machine (UTM).

Mode I fracture tests were conducted using the miniature compact tension (CT) specimens (dimensions given in Fig. S1(a) are machined from the ingots in both as-cast and CTC condition using wire cut EDM. The root diameter of the U-shaped notches (15.1 mm deep) that are introduced in these specimens via wire-cut EDM is ~100 μm. Side surfaces of the specimens are mechanically polished to a mirror-like surface finish. Prior to testing, the locations above and below the centre of curvature of the notch were marked by visible nanoindents. Fracture tests are performed using the Shimadzu UTM at a constant crosshead displacement rate of 0.002 mm/s. Side surfaces and fracture surfaces of the tested specimens are examined in a SEM. In our previous study, we have reported the mode I fracture behaviour of the as-cast BMGC bar (referred to as CD-NT in the previous paper) [32]. Therefore, the relevant fracture data of as-cast BMGC bar is reproduced and cited where relevant in this paper.

3. Results

3.1. Microstructure and mechanical characterization of as-cast BMGC ingot and bar

Representative microstructures of the as-cast BMGC ingot and bar specimens are displayed in Figs. 1(a) and 1(b), respectively. Both contain a dark matrix embedded with dendrites of lighter contrast. Differences in the contrasts of the two phases are an outcome of their compositional

differences. Some needle-like features with darker contrast are observed in the matrix of the ingot specimen but the same was not seen in the bar specimen. The EDS composition maps obtained from the as-cast BMGC ingot and bar specimens are displayed in Fig. S3(a) and S3(b), respectively. While the dendrites are rich in Nb and lean in Cu, the converse is true for the matrix. The overall chemical compositions of the dendrite and matrix are $Zr_{53.7}Ti_{28.6}Nb_{16}Cu_{1.7}$ and $Zr_{61}Ti_{19.9}Nb_{6.1}Cu_{12}$, respectively in both BMGCs (Beryllium is not detected by EDS). In Figs. 1(c) and 1(d), the composition line scans across the dendrites and matrix of the as-cast ingot and bar specimens, respectively, are displayed. The distribution of all constituents in the dendrite and matrix of as-cast bar appears to be uniform. A similar uniformity in the distribution of the constituents within the dendrite is observed for the as-cast ingot. However, the line scan along the amorphous matrix portion indicates sharp fluctuations in the compositions of Cu, Zr, and Ti. In locations where the relative concentration of Cu and Zr are higher by 5 wt%, the Ti concentration is lower and vice versa. This implies that these constituents tend to micro-segregate within the amorphous phase.

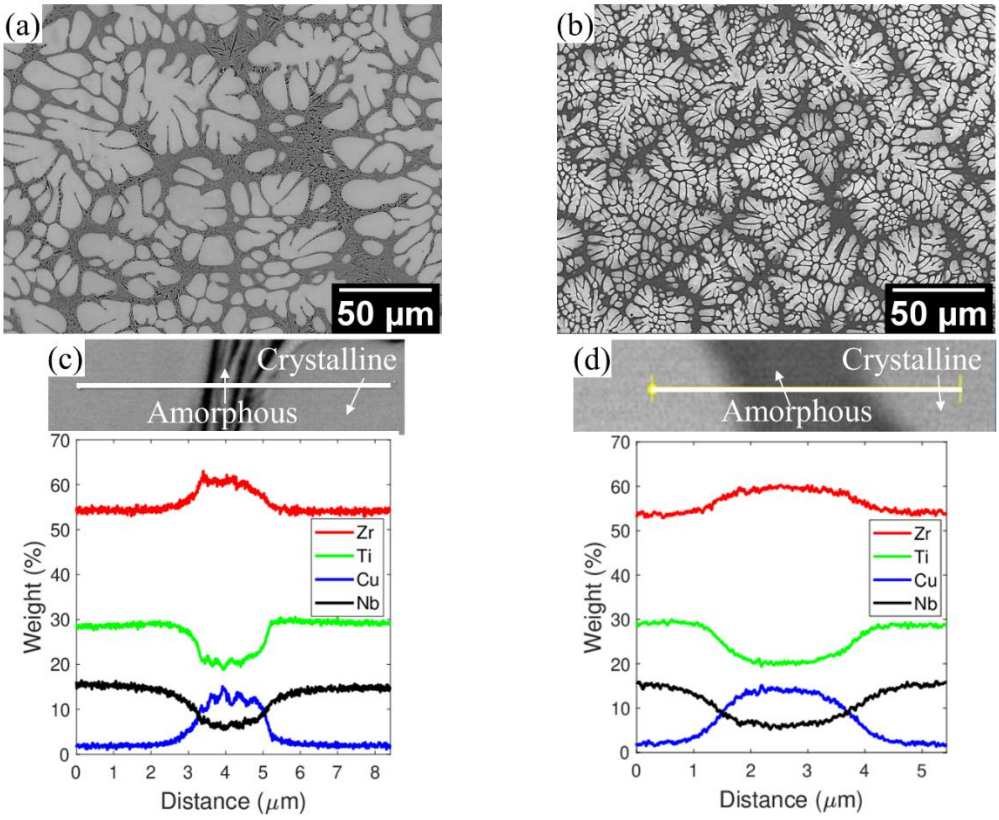

Fig. 1. *Representative microstructures of the (a) as-cast ingot and (b) as-cast bar specimens. Composition line scans of these specimens are shown in (c) and (d), respectively.*

From the image analyses of the microstructures, the volumetric fraction of dendrites, V_d, in both the ingot and rod BMGCs was estimated to be 62.8±2.1%. The average dendrite arm size, Ω, and interdendritic spacing, λ, in the ingots are 37.4 ± 11.5 μm and 30.2 ± 6.1 μm, respectively. They are 7 ± 1.89 μm and 6.81 ± 0.95 μm in the bar specimens. Microstructure analyses are done using ImageJ software. These significant difference in Ω and λ are an outcome of the differences in the effective cooling rates experienced by them during casting. Since the dimensions of the ingot are significantly larger than that of the bar, it experiences a lower cooling rate than the bar specimens. As lower cooling rate promotes faster growth of the precipitating phase, the ingot expectedly has higher Ω and λ.

No significant differences between the XRD scans of the as-cast ingot and bar specimens could be seen, which is shown in Fig. 2. Both show the presence of sharp peaks corresponding to the body centered cubic (bcc) crystalline phase (β-Ti dendrites) superimposed over a broad hump associated with the amorphous phase (BMG matrix). The absence of additional peaks in the scans of the as-cast ingot specimen indicates that the dark needle like features are either a non-crystalline feature or secondary β-Ti, which forms in the BMG matrix at low cooling rates. If the latter is the case, the peaks of secondary β-Ti would overlap with those of primary β-Ti dendrites. Since no other phases were detected in the ingot, a dual-morphology β-Ti microstructure is highly likely [43].

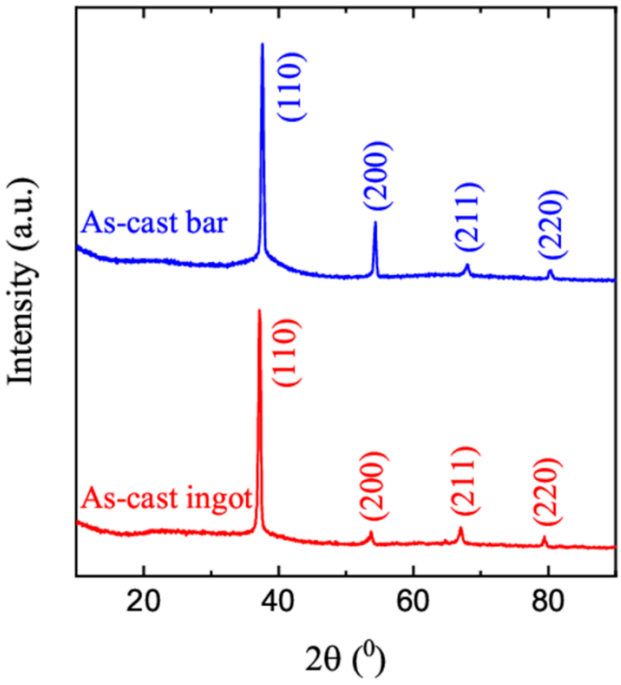

Fig. 2. *XRD scans of the as-cast ingot and as-cast bar specimens.*

Representative engineering stress, σ, vs. engineering strain, ε, responses of the as-cast ingot obtained during the tensile tests is displayed in Fig. 3. In the same plot, the tensile σ-ε data of the as-cast bar, reported in our previous study [32], is included for comparison. Both have similar Young's modulus, *E*, yield strength, YS, and, ultimate tensile strength, UTS, of ~105.16 GPa, ~1085.6 MPa, and ~1123.1 MPa, respectively. In contrast, the strain-to-failure, ε_f, of the ingot is only ~1.8%, whereas that of the bar is 10% with strain hardening observed up to ε ~4%, followed by necking, and considerable post necking elongation. The negligible plasticity in the ingot suggests that it is brittle, although its V_d and phase composition are identical to those of the bar. Considering the brittle nature of the as-cast ingot, an attempt is made to modify its structural state via CTC treatments, with the intention of enhancing its plasticity.

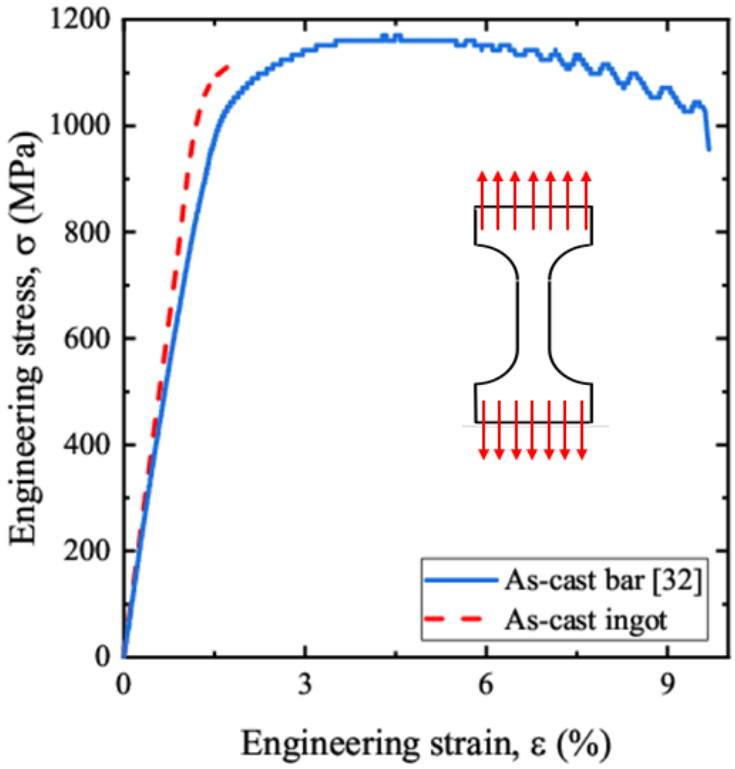

Fig. 3. *Uniaxial tensile stress-strain (σ-ε) responses of the as-cast ingot and bar specimens. (Data of the bar specimens is taken from ref. [32].)*

3.2. Structural state and mechanical heterogeneity of as-cast and CTC treated BMGCs

The DSC scans obtained on the as-cast ingot and bar specimens are displayed in Fig. 4(a) along with those obtained on the ingot specimens subjected to CTC cycles. With increasing temperature, an endothermic region that corresponds to the glass transition, followed by a supercooled liquid region, and an exothermic peak that corresponds to crystallization is seen in all the scans. The glass transition temperature, T_g, in all cases is ~625 K. The area under the exothermic hump before the glass transition corresponds to the enthalpy of relaxation, ΔH_{rel}, of the amorphous matrix and is the energy difference between its 'as quenched' and relaxed states. ΔH_{rel} is often taken as a quantitative measure of the glass's structural state [44,45]. A lower ΔH_{rel} indicates a structurally relaxed amorphous phase that is nearer to the ideal (equilibrium) glass state. Variations of ΔH_{rel} in the ingot specimens as a function of N_{CT} are displayed in Fig. 4(b). The as-cast ingot (N_{CT} = 0) and the as-cast bar have ΔH_{rel} of 3.97 ± 0.16 and 10.44 ± 0.31 J/g,

respectively. Clearly, the matrix phase in the ingots is far more structurally relaxed than that in the bars. With increasing N_{CT}, ΔH_{rel} increases—but non-monotonically. At N_{CT} ~ 5, ΔH_{rel} increases to almost twice of that of the as-cast ingot.

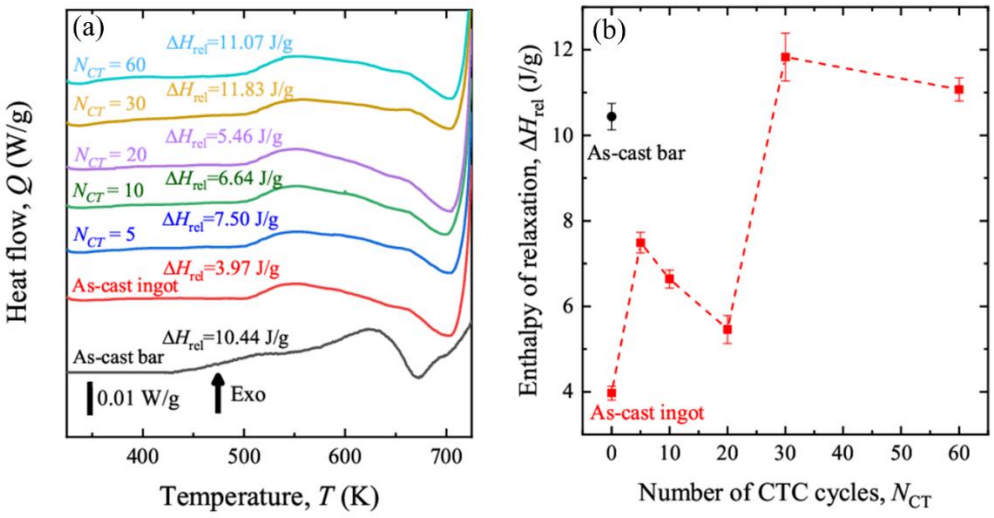

Fig. 4. *(a) DSC plots obtained on bar and ingot specimens in the as-cast and cryothermal cycling (CTC) states. (b) Variation in enthalpy of relaxation, ΔH_{rel}, with the number of CTC cycles, N_{CT}.*

Possible mechanical heterogeneity within the amorphous matrices of as-cast bar and ingot specimens, and the CTC ingots, is investigated by recourse to the spherical-tip nanoindentation experiments. A representative indentation load, P, vs. displacement, h, response of the amorphous matrix of a BMGC is displayed in Fig. 5(a). The P-h response is initially elastic and consistent with that predicted by Hertzian elastic contact theory [46], and is given by

$$\boldsymbol{P = \frac{4}{3} E_r \sqrt{R_i} \cdot h^{\frac{3}{2}}} \tag{1}$$

where, E_r is reduced modulus, and R_i is the radius of the indenter tip. E_r accounts for the deformation under the applied load in the specimen as well as the indenter tip. Young's modulus of the specimen, E_s, is given by the relation [46],

$$\boldsymbol{\frac{E_s}{1-\nu_s^2} = \left(\frac{1}{E_r} - \frac{1-\nu_i^2}{E_i}\right)^{-1}} \tag{2}$$

where, ν_i and ν_s are the Poisson's ratios of indenter tip and specimen, respectively. The elastic to elasto-plastic transition is marked by a 'pop-in' or a discrete displacement burst. The maximum shear stress at the first pop-in, τ_{max}, corresponds to the incipient shear strength of the indented material [47–50] and is related to the first pop-in load, P_I, through

$$\boldsymbol{\tau_{max} = 0.31\left(\frac{6E_r^2}{\pi^3 R_i^2}P_I\right)^{\frac{1}{3}}}. \quad (3)$$

Cumulative probability distributions of τ_{max} for as-cast ingot, bar and CTC ingots are displayed in Fig. 5(b). While τ_{max} has a wide distribution in all cases, its range varies depending on the structural state of the BMGC. The mean, $\boldsymbol{\bar{\tau}_{max}}$, and the coefficient of variation, CV, which is defined as the ratio of the standard deviation and the mean of τ_{max} are listed in Table 1. For the as-cast bar and ingot, $\boldsymbol{\bar{\tau}_{max}}$ are ~3.7 and 1.79 GPa, respectively. No specific trend in $\boldsymbol{\bar{\tau}_{max}}$ vs. N_{CT} could be identified. For the as-cast bar and ingot specimens, CVs are 0.22 and 0.26, respectively. In CTC ingots, CV varies non-monotonically with increasing N_{CT}, much like ΔH_{rel}. Both CV and ΔH_{rel} peak at N_{CT} ~30.

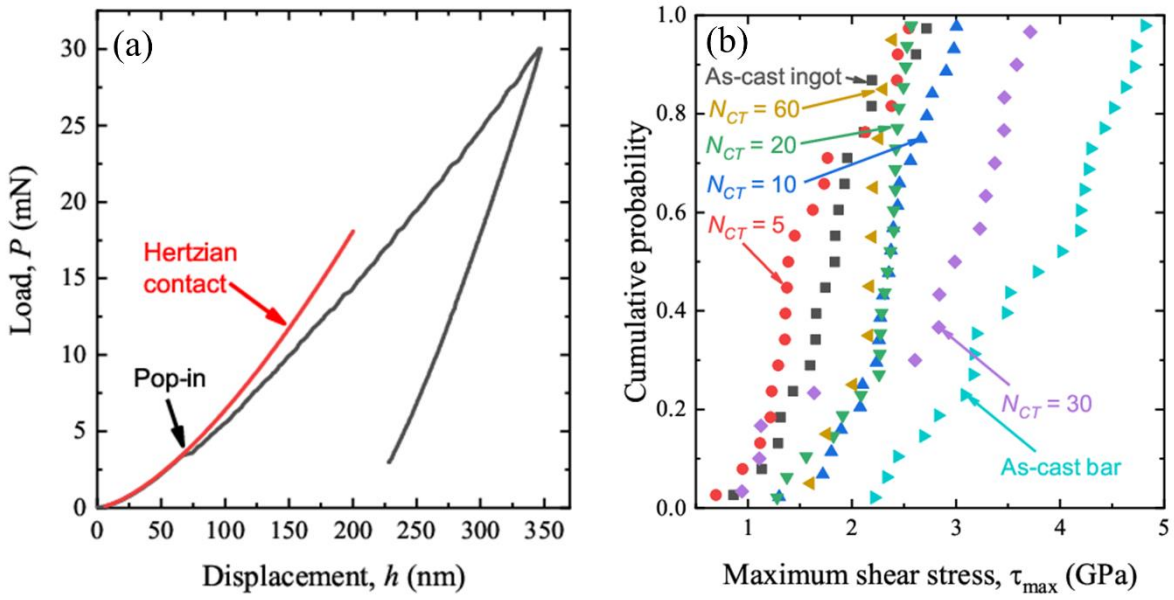

Fig. 5. *(a) Representative indentation load-displacement (P-h) response measured on the matrix phase of a composite. (b) Cumulative probability distribution of maximum shear stress, τ_{max}, obtained on the bar and ingot specimens in the as-cast and CTC states.*

Table 1. Summary of mechanical properties of as-cast and CTC treated BMGC specimens.

Material stock	Condition	Mean of first pop-in stress, $\bar{\tau}_{max}$ (GPa)	Standard deviation of first pop-in stress (GPa)	Coefficient of variation, CV	Number of pop-ins, N_{pop-in}
Bar	As-cast	3.7	0.81	0.22	13 ± 3
Ingot	As-cast	1.79	0.46	0.26	3 ± 1
Ingot	CTC (5 cycles)	1.6	0.53	0.33	6 ± 2
Ingot	CTC (10 cycles)	2.35	0.41	0.17	9 ± 2
Ingot	CTC (20 cycles)	2.22	0.35	0.16	11 ± 1
Ingot	CTC (30 cycles)	2.68	0.94	0.35	11 ± 1
Ingot	CTC (60 cycles)	2.1	0.24	0.11	4 ± 1

Ketov et al. [45] also reported similar dispersions in τ_{max}. According to them, a higher CV signifies greater mechanical heterogeneity. They assert that such enhanced heterogeneity, in turn, leads to a relatively higher propensity of shear band nucleation in the amorphous alloys subjected to CTC [45]. To assess this, the average number of pop-ins up to P_{max}, N_{pop-in}, in the *P-h* curves of the as-cast bar, ingot, and CTC ingots are carefully counted and listed in Table 1. N_{pop-in} is a direct measure of the propensity to form shear bands, as each pop-in during indentation corresponds to the nucleation of a shear band in the amorphous phase [50].

The as-cast bar has the highest N_{pop-in} ~13 ± 3, whereas it only is 3 ± 1 for the as-cast ingot. However, for the CTC treated BMGC ingots, the N_{pop-in} first increases and then decreases, with increasing N_{CT}. For instance, at N_{CT} ~5 and 10, N_{pop-in} increases to 6 ± 2 and 9 ± 2, respectively. N_{pop-in} further increases to 11 ± 1 for N_{CT} ~20 and remains the same for N_{CT} ~30. However, when N_{CT} ~60, N_{pop-in} reduces markedly to ~4 ± 1. CV and N_{pop-in} appear to be uncorrelated apart from the precipitous drop in their magnitudes for N_{CT} > 30. This suggests that determining the propensity of shear band nucleation from the magnitude of CV or enhanced mechanical heterogeneity may not necessarily be equivalent.

Overall, it is observed that ΔH_{rel}, CV, and N_{pop-in} are highest at N_{CT} ~30, which implies that the ingot BMGC subjected to 30 thermal cycles has the highest propensity to undergo shear band mediated flow. Coincidentally, a significant enhancement in plasticity of the amorphous phase was also observed for N_{CT} ~30 by Ketov et al. in their study on Zr-based BMGs [45].

Therefore, subsequent investigations are performed only on ingots subjected to 30 thermal cycles, which will hitherto be referred to as 'CTC-30 ingot'.

3.3. Microstructure and mechanical properties of CTC-30 BMGC ingot

A representative microstructure and the composition map of the CTC-30 ingot are displayed in Fig. 6(a) and Fig. S4, respectively. Note that the dendrite composition, V_d, Ω, and λ in this BMGC is same as that of as-cast ingot. As expected, CTC did not affect the composition or other characteristics of the dendritic reinforcements of the BMGC. Fig. 6(b) shows the EDS line scan across the dendrite and matrix of the CTC-30 ingot. The variations in compositions of different constituents in the matrix and dendrite resemble that what is seen in as-cast BMGC ingot (see Fig. 1(c)), i.e., all the constituents are uniformly distributed in the dendrite, but Cu, Zr and Ti exhibit composition fluctuations of the order of ~5 wt% in the amorphous phase. Also, Cu and Zr appear to microsegregate together in Ti-lean regions and vice versa. However, it is noteworthy that the widths of the microsegregated regions in CTC-30 ingot appear to be significantly larger than that in the as-cast ingot. However, the matrix of CTC-30 ingot also does not undergo any phase changes as its XRD scan, shown in Fig. 6(c), is identical to that of the as-cast ingot.

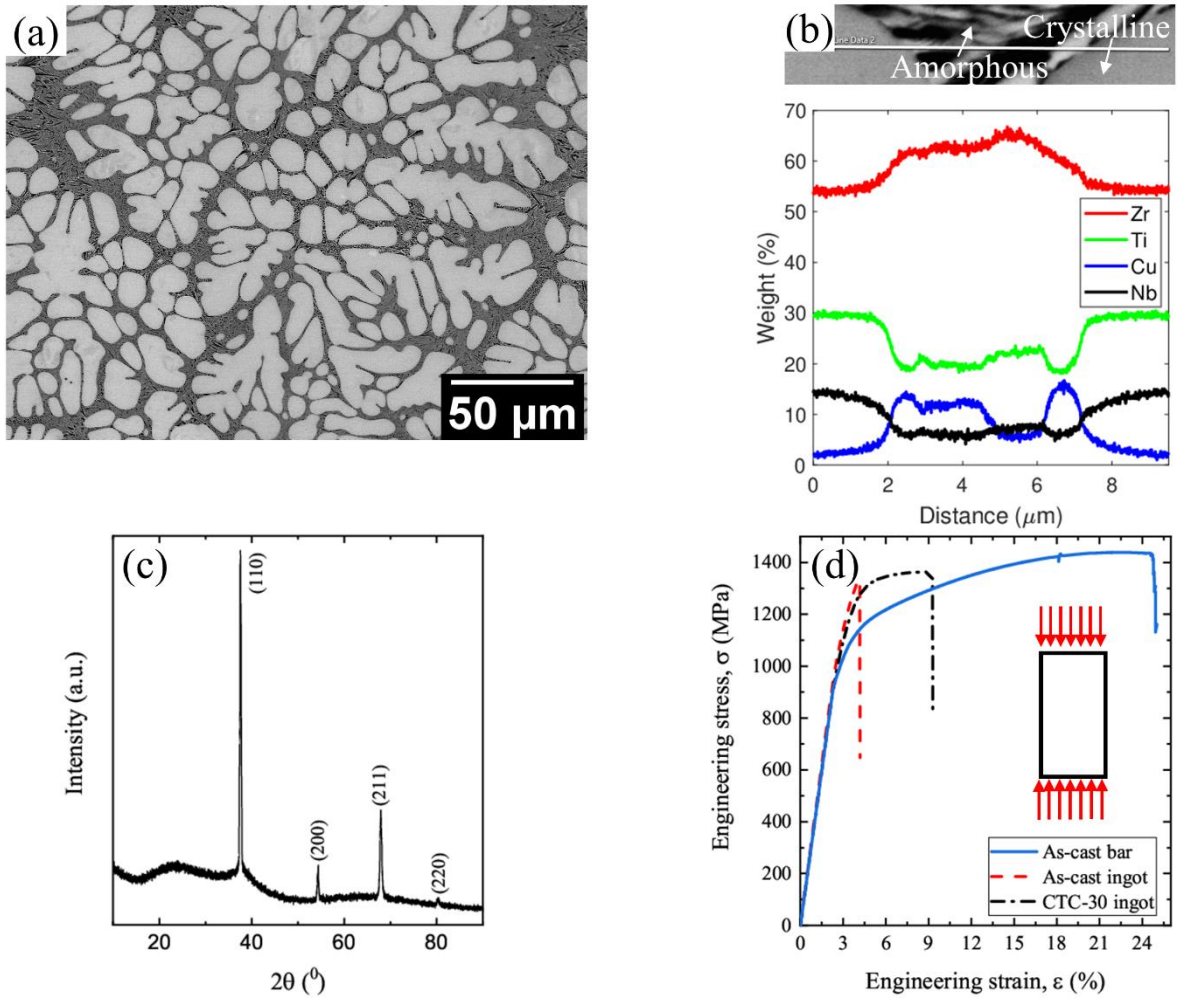

Fig. 6. *(a) Representative microstructure of the ingot specimen that was cryothermal cycled (CTC) 30 times. (b) Compositional line and (c) XRD scans obtained across it. (d) Compressive σ-ε responses of the as-cast bar and ingot specimens, and the CTC-30 ingot specimen.*

The uniaxial compression responses of the as-cast bar and ingot, and CTC-30 ingot are compared to further assess their mechanical properties. Compression tests, instead of tension tests, are preferred in view of the possibility that they may reveal subtle differences in plasticity—if any—of the examined composites. Representative σ-ε responses are displayed in Fig. 6(d). While all the three BMGCs have the same *E*, their YS, UTS, and ε_f vary considerably. The as-cast bar specimens have YS and UTS of ~1082 ± 12 and 1442 ± 6, respectively. The similarity of YS measured in uniaxial tension and compression indicates that these BMGCs do not exhibit significant tension-compression asymmetry, which has also been observed by others [16,51]. YS of the as-cast and CTC-30 ingots are similar but are ~200 MPa higher than that of

the as-cast bar. The as-cast ingot specimens failed immediately after yielding whereas the CTC-30 ingot specimens deformed plastically to ε_f ~10% and attain a UTS of ~1360 MPa, before failing. Note that the as-cast bar has 2.5 times higher ε_f than that of the CTC-30 ingot, i.e., while CTC-30 ingot has enhanced strength compared to the as-cast bar, it undergoes considerably lesser plastic deformation than the latter but more than the as-cast ingot. Figs. 7(a)-(c) show SEM images of the side surfaces of the compression-tested specimens of the as-cast bar and ingot, and CTC-30 ingot, respectively. While several shear bands were found on the surfaces of the as-cast bar, none were observed in the other two.

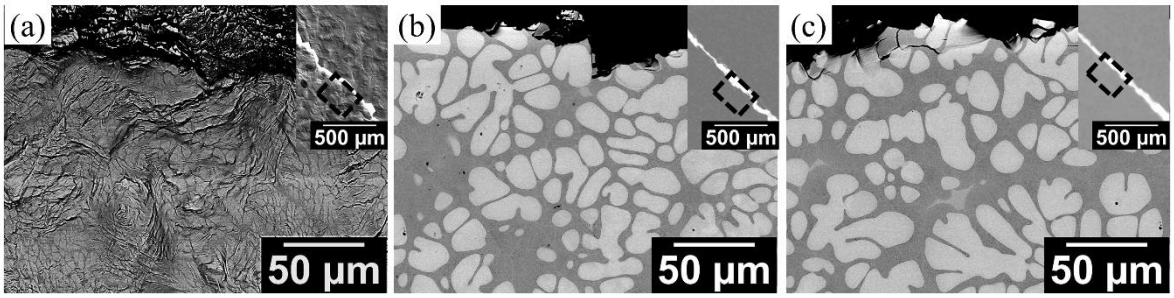

Fig. 7. *Microstructures of the compression-tested (a) as-cast bar, (b) as-cast ingot, and (c) CTC-30 ingot specimens. Insets in (a), (b), and (c) are low magnification SEM images of the respective specimens.*

To further understand the evolution of plasticity in these BMGCs, Vickers indentations were performed on them. The measured hardness, *H*, of the as-cast ingot is 7.18 ± 0.05 GPa, whereas that of the CTC-30 ingot is marginally lower at 6.73 ± 0.15 GPa. In contrast, the as-cast bar's *H* is significantly lower at 3.33 ± 0.03 GPa. Optical images of the Vickers indents are displayed in Fig. 8. Around the indent on as-cast bar, several curved shear bands can be observed. The average number of shear bands, N_{sb}, is ~18. However, instead of shear bands, cracks appear to form around the indents of the as-cast and CTC-30 ingot specimens (marked by white and red arrows in the images), attesting to their brittle nature. Overall, the results of the compression and Vickers indentation tests suggest that the as-cast bar is amenable to plasticity through the shear band mechanism, but the as-cast and CTC-30 ingot, which are comparatively stronger and harder, undergo only cracking. These observations are in contrast to those made via the nanoindentation tests, where $N_{pop\text{-}in}$ of the CTC-30 ingot and as-cast bar specimens are somewhat similar.

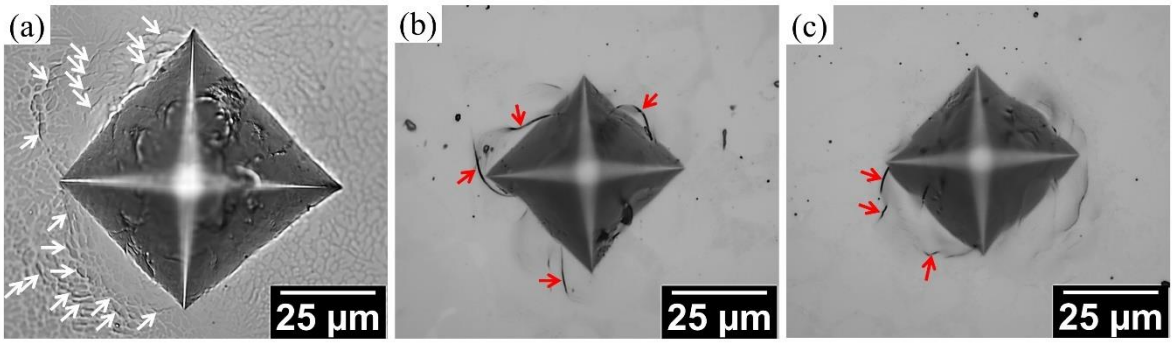

Fig. 8. *Optical micrographs of the Vickers indents on (a) as-cast bar, (b) as-cast ingot, and (c) CTC-30 ingot specimens.*

3.4. Fracture of as-cast and CTC-30 ingot

During the mode I fracture tests on the as-cast and CTC-30 ingot specimens, the load, F, initially increases linearly with load point displacement, δ, followed by fracture at $F \sim 623.7$ and 598.5 N, respectively. Real time videos of the notch tip during fracture tests in both ingot specimens are shown in Movies S1 and S2. SEM images of the notch tip regions of the fractured specimens are displayed in Fig. 9. In the as-cast ingot specimen, the crack propagates parallel the notch line whereas it propagates at +45° in the CTC-30 specimen. The convention for measuring the angle ϕ from the notch line and results of the mode I fracture tests on the as-cast bar specimens are provided in our earlier work [32]. It is observed that the notch tips of the as-cast bar specimens exhibit significant blunting prior to fracture and are surrounded by a dense envelope of shear bands that are concentrated within five distinct lobes originating from the notch tips (Fig. 6 of ref. [32]). In contrast, no shear bands are observed at the notch tips of both the as-cast and CTC-30 ingot specimens (see Movies S1 and S2). Importantly, while the crystalline dendrites in the as-cast bar successfully arrest the cracks in the amorphous matrix from propagating [29,32], the same is not observed in either of the ingot specimens.

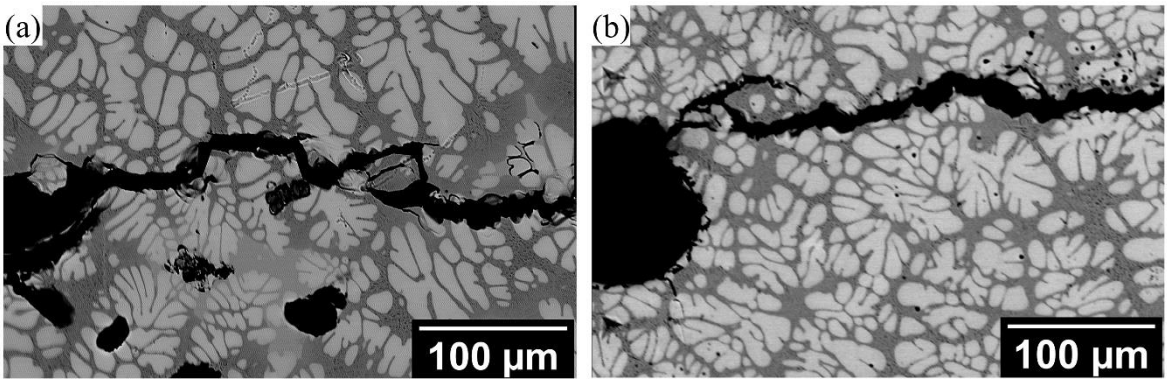

Fig. 9. *Scanning electron micrographs of the notch tip regions of the mode I fracture tested (a) as-cast and (b) CTC-30 ingot specimens.*

In the absence of an incipient crack in the ingot specimens, the notch toughness, K_{QJ} is calculated from the method detailed in section S1 of the supplementary information (SI). For the as-cast and CTC-30 ingot specimens, K_{QJ} is ~35.2 and ~33 MPa.m$^{0.5}$, respectively. In the as-cast bar specimen, although a crack nucleates at the notch tip, plane strain fracture conditions are not met and a conditional fracture toughness, K_Q ~157 MPa.m$^{0.5}$, is determined [32]. A comparison between the K_{QJ} of ingot specimens and K_Q of bar specimen, though strictly not correct, indicates that as-cast bar is at least 5 times tougher than both the ingot specimens. Importantly, CTC does not lead to an enhanced toughness!

Low magnification fractographs of the as-cast and CTC-30 ingot specimens are displayed in Figs. 10(a) and 10(b), respectively. White dashed lines indicate the position of the notch front in both the specimens, whereas arrows indicate the direction of crack propagation. The fracture surfaces of both ingot specimens are undulated and exhibit rough features. In contrast, the as-cast bar specimens, exhibit two distinct fracture morphologies (see Fig. 11 in ref. [32]). Just ahead of the notch front, there is a distinct fluid meniscus instability (FMI) zone that has a width of ~95 µm [32]. This zone, which is otherwise flat and featureless, contains micrometer-sized ridges that extend parallel to the direction of crack growth. Beyond this zone, the fracture surfaces are undulated and rough and contain ductile fracture features such as vein patterns (see Fig. 11 in ref. [32]). These results indicate that as-cast and CTC-30 ingots are equally brittle from the point of view of fracture toughness compared to the as-cast bar specimen.

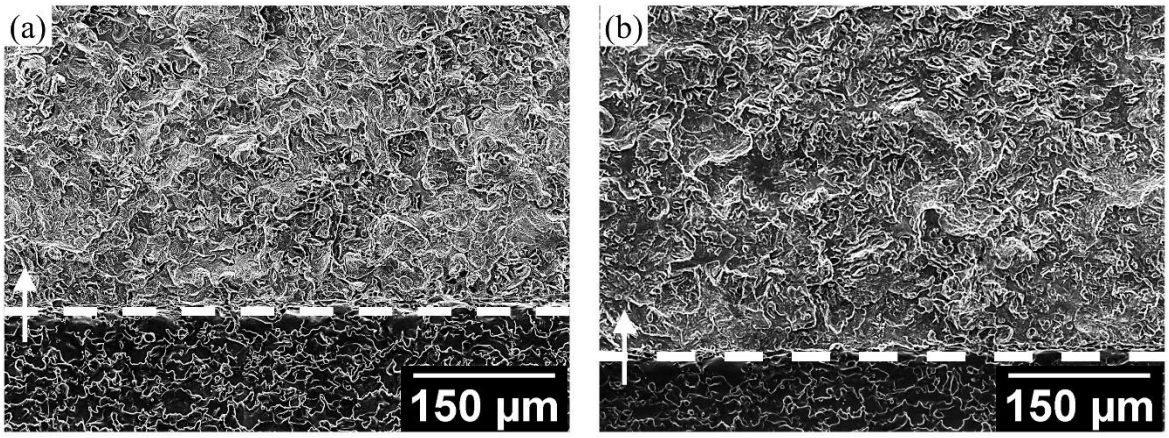

Fig. 10. *Scanning electron micrographs of the fracture surfaces of the (a) as-cast and (b) CTC-30 ingot specimens tested in mode I configuration.*

4. Discussion

4.1. Fracture mechanisms

In an earlier study, we reported that the fracture mechanisms in 'ductile' BMGs and BMGCs of comparable compositions are broadly similar [32]. In both the materials, formation of several curved shear bands, whose shapes and spacial extent are determined by elasto-plastic stress gradients ahead of the notch tip is noted [32,52–56]. Some subtle differences in the shear band characteristics exist, however. In the monolithic BMGs, the bands are continuous and are accompanied by large shear offsets. In BMGCs, in contrast, they are short, discontinuous, and have relatively smaller offsets, all of which are a result of the hindrance provided by the β-Ti to the shear band propagation [29,32]. Stable crack nucleation still occurs within the dominant shear band, just as in monolithic BMGs, when the plastic strain, ε_p, within one of the shear bands exceeds a critical value. Tandaiya et al. [52] calculated the strain fields ahead of the notch tip in a Zr-based BMG and determined that ε_p reaches a maximum at $\phi \sim \pm 69°$ from the notch line. This implies that a shear band oriented at this ϕ from the notch line will transition into a crack. In BMGCs, crack nucleation within a shear band occurs at a lower ϕ of $\sim \pm 56°$. This difference in ϕ for BMG and BMGCs is possibly due to the additional plastic constraint imposed by the presence of dendrites in the latter's matrix. In both BMGs and BMGCs, further loading leads

limited stable crack growth, which is immediately followed by fracture. The similarities in fracture mechanisms and fracture criterion are further supported by the observation of a distinct FMI zone near the notch front of their fracture surfaces, which indicates that stable crack growth has occurred within the dominant shear band.

Despite the above, BMGCs have significantly higher K_{IC} (or K_Q) than BMGs [29,32]. This is attributed to the formation of several more shear bands, with shallower offsets, in them. This reduces the heterogenous nature of plasticity at the notch tip and delays crack initiation. While this ductile fracture mechanism is applicable to the as-cast BMGC bars, our results indicate that it may not be the case for the as-cast and CTC-30 ingot specimens, which exhibit brittle fracture characteristics.

Narayan et al. [57] performed mode I fracture tests on a structurally relaxed Zr-based BMG and reported that fracture occurs without the formation of shear bands ahead of the notch tip. Moreover, its K_{IC} (~11 MPa.m$^{0.5}$) is 5 times lower than that of its as-cast counterpart. Given the absence of notch tip plasticity in ingot specimens and the marked difference in K_{QJ} compared to the bar specimen, the fracture mechanisms in them and brittle BMGs are expected to be broadly similar.

Fracture in brittle BMGs occurs when the stress exceeds the critical cavitation stress of the material over some distance ahead of the notch tip [52]. Subsequently, crack propagation is accompanied by the formation of nanoscale cavities, which coalesce and form periodic nanocorrugations on the fracture surface [1]. The fracture surface of a BMG that underwent brittle fracture is macroscopically flat and featureless [57–60]. In contrast, the fracture surfaces of the as-cast and CTC-30 BMGC ingot are not flat and contain rough features (see Fig. 10). It is likely that these differences in fracture features are an outcome of the plastically deforming dendrites in the latter.

4.2. Origin of embrittlement of the as-cast and CTC-30 ingot specimens

The origin of embrittlement in the as-cast BMGC ingot appears to be due to the structural relaxation of the amorphous matrix phase. As mentioned earlier, since the cast volume of it is significantly higher than that of the bar, it cools at a lower rate (see section 3.1). Prior studies have shown that BMGs undergo embrittlement due to prolonged sub-T_g annealing or during

solidification from the melt at lower cooling rates [3,29,61–66]. In both the conditions, the amorphous phase experiences higher temperatures for a significantly longer time, which provides sufficient time for the structure to relax and transition to a more stable energetic state or, in the context of the potential energy landscape theory, occupy a deeper energy minimum [1,67]. In contrast, faster cooling minimizes structural relaxation, and the BMG is much more structurally disordered. Note that greater structural relaxation lowers the free volume content in a BMG, which in turn, influences its plasticity. Plasticity in BMGs is accommodated by clusters of atoms that collectively undergo a shear transformation, and are hence referred to as shear transformation zones (STZs) [1,68–71]. The activation of several of these STZs results in the formation of a macroscopic shear band in the material. However, STZs can operate relatively easily and with relative ease only when there is sufficient free volume associated with it [72]. If the free volume associated with STZs is insufficient, as in the case of structurally relaxed BMGs, shear bands do not form during deformation and the material exhibits brittle behaviour.

While the brittleness of as-cast ingot is possibly due to structural relaxation of its BMG matrix, it is surprising that the CTC-30 ingot also exhibits the same levels of toughness, i.e., it does not enhance the toughness in any marked manner. Li et al. [42] and Ketkaew et al. [41] studied the variations of fracture toughness of monolithic BMGs in the as-cast and CTC conditions and concluded that K_{IC} increases by ~50% if the material is subjected to an appropriate number of thermal cycles. They mentioned that the appropriate number of cycles corresponds to the state where BMGs exhibit significant shear band mediated plasticity. Ketov et al. [45] suggested that significant shear band mediated plasticity is observed when the ΔH_{rel} of the BMG and the dispersion of τ_{max} at first pop-in--measured as CV in this study--are relatively high. They reasoned that higher dispersion of τ_{max} implies that there are several hard and soft spots in the amorphous phase. The soft spots nucleate shear bands whereas the hard spots resist their propagation. Such a distribution of hard and soft spots in the amorphous phase would promote formation of multiple short shear bands and homogenize plastic flow [1,45,73,74]. Similarly, since ΔH_{rel} is proportional to the free volume content, its higher value would imply that the BMG is capable of activating a significantly higher number of STZs, which in turn, would facilitate the nucleation of multiple shear bands [44]. Extending this concept to BMGCs, we expected that the CTC-30 ingot would exhibit enhanced K_{IC} compared to the as-cast ingot as it exhibits a reasonable plastic strain-to-failure of ε_f ~10% in compression, and its amorphous

matrix exhibits highest $N_{pop\text{-}in}$, and largest CV of τ_{max} in spherical nanoindentation. Moreover, the ΔH_{rel} of the CTC-30 ingot is even higher than that of as-cast bar. However, this local plasticity enhancement did not translate to enhanced crack tip plasticity and improvement in K_{IC}, which is contrary to our (and prior studies) expectations. We explore the reasons for this, below.

First, it is important to assess if the estimation of plasticity from $N_{pop\text{-}in}$, and CV of τ_{max}, obtained from the spherical nanoindentation test, is reliable. Note that a pop-in in the *P-h* curve, regardless of the material indented, appears when there is instantaneous relaxation of strain at a fixed load. For instance, in certain brittle materials, the nucleation of dislocations or the formation of a crack leads to pop-ins [46,75]. In BMGs, while a pop-in is implicitly assumed to be a signature of shear band nucleation, it is not necessarily always true. Raghavan et al. [63] have shown that in structurally relaxed BMG, cracks form around the edges of Vickers indents. The formation of these cracks coincides with the observation of pop-ins in their nanoindentation *P-h* curves. Similarly, since cracks are also observed around the Vickers indents on CTC-30 ingot (see Fig. 8), there is a strong reason to believe that the BMG matrix of the CTC-30 ingot is also structurally relaxed and that the pop-ins observed in their nanoindentation *P-h* curve correspond to nucleation of microcracks and not shear bands. The absence of shear bands in the compressed as-cast and CTC-30 ingot also confirms this (see Figs. 7(b)and 7(c)). This also means that utilizing either of $N_{pop\text{-}in}$, and CV of τ_{max} from nanoindentation tests to assess the extent of shear band mediated plasticity is reliable only if it is confirmed that the BMG or the amorphous matrix of BMGCs is capable of nucleating shear bands. In essence, the utilization of nanoindentation testing to characterize the structural state of the amorphous phase, in isolation, is not recommended and needs to be supplemented by an alternate measurement of structural disorder. For that reason, most studies rely on the measurement of ΔH_{rel}, which provides a quantitative estimate of structural disorder in terms of the free volume. However, in this study, the magnitude of ΔH_{rel} also fails to reliably indicate the extent of plasticity of the BMG matrix in the CTC-30 ingot.

To understand the reason for this, we examine the atomic structure changes associated with the enthalpy of relaxation in BMGs. Van den Beukel and Radelaar [76] have shown that ordering of atoms in BMGs can be classified in terms of topological short range order (TSRO) and chemical short range order (CSRO). While the extent of TSRO depends exclusively on

geometrical packing and space filling, CSRO originates from the mutual affinity of certain constituents in a multi-component BMG. It can then be visualized that a higher degree of TSRO, which corresponds to effective space filling, will result in lower free volume and vice versa, whereas no such direct correlation exists between CSRO and the free volume [77]. This is because the driving force for CSRO, which manifests as micro-segregation of certain constituents, is energy minimization via the formation of symmetric polyhedral structures [78]. While higher symmetry structures are thermodynamically stable, they may not necessarily be close packed. Therefore ΔH_{rel}, which is a measure of the free volume, accurately captures variations in the TSRO, but not of CSRO.

The relative extents of CSRO and TSRO is a good metric to understand the structural state and its influence on the plastic deformation of the amorphous matrix in the BMGCs considered in this study. Since the as-cast bar appears to have a uniform distribution of constituents in its amorphous phase, the extent of CSRO is minimal and TSRO sufficiently describes its structural order.

Alternately, microsegregation of Cu and Zr in the matrix of as-cast ingot (see Fig. 1(c)) indicates that the atoms have enhanced CSRO. Moreover, prior studies have shown that Cu and Zr have considerable mutual affinity as they form a highly symmetric icosahedral structure, which has the Voronoi indices <0, 0, 12, 0> [79–85]. It is also observed that the number density of this icosahedral structure increases with increasing annealing times or decreasing cooling rates (during solidification from the melt). These icosahedral structural units, to preserve their structural symmetry, resist shear transformations and do not accommodate local plastic strain. This implies that in the amorphous phase that has a greater degree of CSRO, STZ activation will be relatively more difficult. This in turn will restrict the nucleation of shear bands and lead to embrittlement of the amorphous matrix, irrespective of its free volume content (or TSRO).

Based on the above discussion, it is now possible to explain why the increase in ΔH_{rel} of CTC-30 ingot does not correspond to increase in its shear band plasticity. Although the CTC treatment for 30 cycles on as-cast ingot enhances ΔH_{rel} or free volume of its amorphous matrix, it still retains the initially microsegregated regions of Cu-Zr and Ti (see Fig. 6(b)). This means that while CTC treatment is capable of altering the TSRO of the amorphous matrix, its effect on

CSRO is negligible. The retention of CSRO in CTC-30 ingot makes it as brittle as the as-cast ingot.

It is then worth asking why Li et al. [42] and Ketkaew et al. [41] reported more than a 50% increase in the K_{IC} of BMGs after a specific number of CTC cycles. Note that the BMGs examined in their studies exhibit a significant degree of plasticity even in its as-cast state. We believe that the CRSO in these BMGs, like the as-cast bar in this study, is negligible. Since CTC only leads to variations in the TSRO, CSRO will never be induced in them. Therefore, K_{IC} variations will be solely governed by the variations in the free volume content or ΔH_{rel}. In contrast, the matrix of the as-cast ingot examined in this study is structurally relaxed to the extent that it underwent CSRO. It then follows that the CTC treatment is effective in modifying K_{IC} only when a BMGs or the amorphous matrix of a BMGC has not undergone CSRO.

In closing, we re-emphasize that the utility of CTC or any alternate rejuvenation treatment for enhancing K_{IC} of BMGs or BMGCs appears to be limited. While there are indications that the structural state of the amorphous phase changes with the number of CTC cycles, if the complete characteristics of the structural state are not considered, one might incorrectly estimate its plasticity and in particular toughness.

5. Summary and conclusions

The microstructure and mechanical properties of a β-Ti reinforced Zr-based BMGC cast into bar and ingot forms are investigated. The ingot undergoes structural relaxation due to its larger size and exhibits negligible ductility and poor toughness. In an attempt to enhance its toughness, 5 sets of CTC treatments with different number of cycles are performed on the ingot. DSC scans indicate that ingot subjected to 30 CTC cycles has the maximum ΔH_{rel} amongst the lot. It also exhibits the greatest scatter in shear yield strength and most number of plastic events, both of which are measured via nanoindentation. Compression tests also confirm that the CTC treated ingot exhibits greater plasticity. Contrastingly, Vickers indentation imprints of both as-cast ingot and the CTC treated ingot are surrounded by cracks, whereas that of the as-cast bar is surrounded by shear bands. Mode I fracture experiments on these BMGCs reveals that as-cast bar specimens have the highest K_{IC}, whereas the toughness of the ingot BMGCs, both in the as-cast and CTC treated forms, is significantly lower, which implies that they are brittle. The reason ingot BMGC

fails to regain its toughness via CTC treatments despite exhibiting high relaxation enthalpy in DSC is because its constituents irreversibly microsegregate during structural relaxation. This could result in the formation of icosahedral structures that are incapable of undergoing shear transformations regardless of the free volume content of the matrix. It is suggested that plastic events observed in the *P-h* curves of nanoindentation could correspond to the nucleation of cracks instead of shear bands. In conclusion, since the CTC rejuvenation treatment only modifies the TSRO of the amorphous phase, its effectiveness in rejuvenating and enhancing the plasticity and toughness of structurally relaxed BMGCs, where CSRO or microsegregation of constituents occurs, is expected to be low.

Acknowledgements

RLN's research at IITD was supported through the Start-up research grant (SRG/2020/000095) of Science and Engineering Research Board, DST, GoI. DR's visit to NTU, where all the experiments reported in this work were conducted, was supported by an IITB-NTU joint PhD Degree Program. The work at Nanyang Technological University was supported by the funding from A*STAR via the Structural Metals and Alloys Programme (No. A18B1b0061). The work at Institute of Metal Research CAS was supported by the National Natural Science Foundation of China (51701213 and 51790484), the National Key Research and Development Program (2018YFB0703402), and the Youth Innovation Promotion Association CAS (2021188).

Declaration of Competing Interest

The authors declare that they have no known competing financial interests or personal relationships that could have appeared to influence the work reported in this paper.

References

[1] C.A. Schuh, T.C. Hufnagel, U. Ramamurty, Acta Mater. 55 (2007) 4067–4109.

[2] U. Ramamurty, S. Jana, Y. Kawamura, K. Chattopadhyay, Acta Mater. 53 (2005) 705–717.

[3] P. Murali, U. Ramamurty, Acta Mater. 53 (2005) 1467–1478.

[4] A.L. Greer, Y.Q. Cheng, E. Ma, Mater. Sci. Eng. R Reports 74 (2013) 71–132.

[5] T. Mukai, T.G. Nieh, Y. Kawamura, A. Inoue, K. Higashi, Scr. Mater. 46 (2002) 43–47.

[6] Z.F. Zhang, J. Eckert, L. Schultz, Acta Mater. 51 (2003) 1167–1179.

[7] J. Xu, U. Ramamurty, E. Ma, JOM 62 (2010) 10–18.

[8] R.L. Narayan, L. Tian, D. Zhang, M. Dao, Z.-W. Shan, K.J. Hsia, Acta Mater. 154 (2018) 172–181.

[9] C. Wang, Q.P. Cao, X.D. Wang, D.X. Zhang, U. Ramamurty, R.L. Narayan, J.Z. Jiang, Adv. Mater. 29 (2017).

[10] D.C. Hofmann, J. Mater. 2013 (2013) 1–8.

[11] H. Choi-Yim, R.D. Conner, F. Szuecs, W.L. Johnson, Acta Mater. 50 (2002) 2737–2745.

[12] C.C. Hays, C.P. Kim, W.L. Johnson, Phys. Rev. Lett. 84 (2000) 2901–2904.

[13] R.L. Narayan, P.S. Singh, D.C. Hofmann, N. Hutchinson, K.M. Flores, U. Ramamurty, Acta Mater. 60 (2012) 5089–5100.

[14] X.Z. Ma, D.Q. Ma, H. Xu, H.Y. Zhang, M.Z. Ma, X.Y. Zhang, R.P. Liu, J. Non. Cryst. Solids 463 (2017) 56–63.

[15] Y. Lu, S. Su, S. Zhang, Y. Huang, Z. Qin, X. Lu, W. Chen, Acta Mater. 206 (2021) 116632.

[16] P.S. Singh, R.L. Narayan, I. Sen, D.C. Hofmann, U. Ramamurty, Mater. Sci. Eng. A 534 (2012) 476–484.

[17] J.W. Qiao, A.C. Sun, E.W. Huang, Y. Zhang, P.K. Liaw, C.P. Chuang, Acta Mater. 59 (2011) 4126–4137.

[18] M.Q. Tang, H.F. Zhang, Z.W. Zhu, H.M. Fu, A.M. Wang, H. Li, Z.Q. Hu, J. Mater. Sci. Technol. 26 (2010) 481–486.

[19] L. Zhang, R.L. Narayan, H.M. Fu, U. Ramamurty, W.R. Li, Y.D. Li, H.F. Zhang, Acta Mater. 168 (2019) 24–36.

[20] L. Zhang, Z. Zhu, H. Fu, H. Li, H. Zhang, Mater. Sci. Eng. A 689 (2017) 404–410.

[21] L. Zhang, R.L. Narayan, B.A. Sun, T.Y. Yan, U. Ramamurty, J. Eckert, H.F. Zhang, Phys. Rev. Lett. 125 (2020) 55501.

[22] D.C. Hofmann, J.-Y. Suh, A. Wiest, G. Duan, M.-L. Lind, M.D. Demetriou, W.L. Johnson, Nature 451 (2008) 1085–1089.

[23] H. Choi-Yim, R. Busch, W.L. Johnson, J. Appl. Phys. 83 (1998) 7993–7997.

[24] R.L. Narayan, K. Boopathy, I. Sen, D.C. Hofmann, U. Ramamurty, Scr. Mater. 63 (2010) 768–771.

[25] D.C. Hofmann, J.-Y. Suh, A. Wiest, M.-L. Lind, M.D. Demetriou, W.L. Johnson, Proc. Natl. Acad. Sci. 105 (2008) 20136 LP – 20140.

[26] L. Tian, R.L. Narayan, K. Zhou, R. Babicheva, U. Ramamurty, Z. Shan, Mater. Sci. Eng. A 818 (2021) 141427.

[27] D. Raut, R.L. Narayan, Y. Yokoyama, P. Tandaiya, U. Ramamurty, Acta Mater. 168 (2019) 309–320.

[28] L. Zhang, S. Chen, H.M. Fu, H. Li, Z.W. Zhu, H.W. Zhang, Z.K. Li, A.M. Wang, H.F. Zhang, Mater. Des. 133 (2017) 82–90.

[29] M.E. Launey, D.C. Hofmann, J.-Y. Suh, H. Kozachkov, W.L. Johnson, R.O. Ritchie, Appl. Phys. Lett. 94 (2009) 241910.

[30] M.E. Launey, D.C. Hofmann, W.L. Johnson, R.O. Ritchie, Proc. Natl. Acad. Sci. 106 (2009) 4986 LP – 4991.

[31] P. Tandaiya, U. Ramamurty, R. Narasimhan, J. Mech. Phys. Solids 57 (2009) 1880–1897.

[32] D. Rajpoot, R.L. Narayan, L. Zhang, P. Kumar, H. Zhang, P. Tandaiya, U. Ramamurty, Acta Mater. (2021) 116963.

[33] S.-C. Lee, C.-M. Lee, J.-W. Yang, J.-C. Lee, Scr. Mater. 58 (2008) 591–594.

[34] H.B. Ke, P. Wen, H.L. Peng, W.H. Wang, A.L. Greer, Scr. Mater. 64 (2011) 966–969.

[35] D.J. Magagnosc, G. Kumar, J. Schroers, P. Felfer, J.M. Cairney, D.S. Gianola, Acta Mater. 74 (2014) 165–182.

[36] Z.Y. Zhang, Y. Wu, J. Zhou, H. Wang, X.J. Liu, Z.P. Lu, Scr. Mater. 69 (2013) 73–76.

[37] Y. Zhang, W.H. Wang, A.L. Greer, Nat. Mater. 5 (2006) 857–860.

[38] S. Di, Q. Wang, Y. Yang, T. Liang, J. Zhou, L. Su, K. Yin, Q. Zeng, L. Sun, B. Shen, J. Mater. Sci. Technol. 97 (2022) 20–28.

[39] P. Xue, S. Pauly, W. Gan, S. Jiang, H. Fan, Z. Ning, Y. Huang, J. Sun, J. Mater. Sci. Technol. 35 (2019) 2221–2226.

[40] P. Xue, Y. Huang, S. Pauly, F. Guo, Y. Ren, S. Jiang, F. Guo, S. Guo, H. Fan, Z. Ning, J.

Sun, J. Alloys Compd. 871 (2021) 159570.

[41] J. Ketkaew, R. Yamada, H. Wang, D. Kuldinow, B.S. Schroers, W. Dmowski, T. Egami, J. Schroers, Acta Mater. 184 (2020) 100–108.

[42] B.S. Li, S. Xie, J.J. Kruzic, Acta Mater. 176 (2019) 278–288.

[43] L. Zhang, S. Pauly, M.Q. Tang, J. Eckert, H.F. Zhang, Sci. Rep. 6 (2016) 19235.

[44] A. Slipenyuk, J. Eckert, Scr. Mater. 50 (2004) 39–44.

[45] S. V Ketov, Y.H. Sun, S. Nachum, Z. Lu, A. Checchi, A.R. Beraldin, H.Y. Bai, W.H. Wang, D. V Louzguine-Luzgin, M.A. Carpenter, A.L. Greer, Nature 524 (2015) 200–203.

[46] U. Ramamurty, J. Jang, CrystEngComm 16 (2014) 12–23.

[47] J.R. Morris, H. Bei, G.M. Pharr, E.P. George, Phys. Rev. Lett. 106 (2011) 165502.

[48] S. Nag, R.L. Narayan, J. Jang, C. Mukhopadhyay, U. Ramamurty, Scr. Mater. 187 (2020) 360–365.

[49] R.L. Narayan, D. Raut, U. Ramamurty, Acta Mater. 150 (2018) 69–77.

[50] G. Singh, R.L. Narayan, A.M. Asiri, U. Ramamurty, Appl. Phys. Lett. 108 (2016) 181903.

[51] M.L. Lee, Y. Li, C.A. Schuh, Acta Mater. 52 (2004) 4121–4131.

[52] P. Tandaiya, R. Narasimhan, U. Ramamurty, Acta Mater. 61 (2013) 1558–1570.

[53] D. Raut, R.L. Narayan, P. Tandaiya, U. Ramamurty, Acta Mater. 144 (2018) 325–336.

[54] P. Tandaiya, R. Narasimhan, U. Ramamurty, Acta Mater. 55 (2007) 6541–6552.

[55] P. Tandaiya, U. Ramamurty, G. Ravichandran, R. Narasimhan, Acta Mater. 56 (2008) 6077–6086.

[56] R.L. Narayan, P. Tandaiya, G.R. Garrett, M.D. Demetriou, U. Ramamurty, Scr. Mater. 102 (2015) 75–78.

[57] R.L. Narayan, P. Tandaiya, R. Narasimhan, U. Ramamurty, Acta Mater. 80 (2014) 407–420.

[58] G. Wang, D.Q. Zhao, H.Y. Bai, M.X. Pan, A.L. Xia, B.S. Han, X.K. Xi, Y. Wu, W.H. Wang, Phys. Rev. Lett. 98 (2007) 235501.

[59] G. Wang, K.C. Chan, X.H. Xu, W.H. Wang, Acta Mater. 56 (2008) 5845–5860.

[60] R. Narasimhan, P. Tandaiya, I. Singh, R.L. Narayan, U. Ramamurty, Int. J. Fract. 191 (2015) 53–75.

[61] P.A. Duine, J. Sietsma, A. van den Beukel, Acta Metall. Mater. 40 (1992) 743–751.

[62] P. de Hey, J. Sietsma, A. van den Beukel, Acta Mater. 46 (1998) 5873–5882.

[63] R. Raghavan, V. V Shastry, A. Kumar, T. Jayakumar, U. Ramamurty, Intermetallics 17 (2009) 835–839.

[64] G. Kumar, D. Rector, R.D. Conner, J. Schroers, Acta Mater. 57 (2009) 3572–3583.

[65] M.E. Launey, R. Busch, J.J. Kruzic, Acta Mater. 56 (2008) 500–510.

[66] Y. Huang, Z. Ning, Z. Shen, W. Liang, H. Sun, J. Sun, J. Mater. Sci. Technol. 33 (2017) 1153–1158.

[67] A.L. Greer, J. Non. Cryst. Solids 61–62 (1984) 737–748.

[68] V. V Bulatov, A.S. Argon, Model. Simul. Mater. Sci. Eng. 2 (1994) 167–184.

[69] M.L. Falk, J.S. Langer, Phys. Rev. E 57 (1998) 7192–7205.

[70] D. Srolovitz, V. Vitek, T. Egami, Acta Metall. 31 (1983) 335–352.

[71] A.S. Argon, H.Y. Kuo, Mater. Sci. Eng. 39 (1979) 101–109.

[72] L. Li, E.R. Homer, C.A. Schuh, Acta Mater. 61 (2013) 3347–3359.

[73] E.S. Park, Appl. Microsc. 45 (2015) 63–73.

[74] J. Ding, S. Patinet, M.L. Falk, Y. Cheng, E. Ma, Proc. Natl. Acad. Sci. 111 (2014) 14052 LP – 14056.

[75] T. Rouxel, J. Jang, U. Ramamurty, Prog. Mater. Sci. (2021) 100834.

[76] A. Van Den Beukel, S. Radelaar, Acta Metall. 31 (1983) 419–427.

[77] M.R.J. Gibbs, H.-R. Sinning, J. Mater. Sci. 20 (1985) 2517–2525.

[78] J. Xu, E. Ma, J. Mater. Res. 29 (2014) 1489–1499.

[79] Y.Q. Cheng, E. Ma, H.W. Sheng, Phys. Rev. Lett. 102 (2009) 245501.

[80] S. Sengul, M. Celtek, U. Domekeli, Vacuum 136 (2017) 20–27.

[81] T. Fujita, P.F. Guan, H.W. Sheng, A. Inoue, T. Sakurai, M.W. Chen, Phys. Rev. B 81 (2010) 140204.

[82] F. Li, X.J. Liu, H.Y. Hou, G. Chen, G.L. Chen, J. Appl. Phys. 110 (2011) 13519.

[83] T. Fujita, K. Konno, W. Zhang, V. Kumar, M. Matsuura, A. Inoue, T. Sakurai, M.W. Chen, Phys. Rev. Lett. 103 (2009) 75502.

[84] A. Foroughi, R. Tavakoli, H. Aashuri, J. Non. Cryst. Solids 432 (2016) 334–341.

[85] X. Hui, H.Z. Fang, G.L. Chen, S.L. Shang, Y. Wang, J.Y. Qin, Z.K. Liu, Acta Mater. 57 (2009) 376–391.